

# **A Frequency Domain Approach for Computing the Lorentz Force in Electromagnetic Metal Forming**

Ruben Otin, Roger Mendez, and Oscar Fruitos

International Center for Numerical Methods in Engineering (CIMNE)  
Parque Mediterráneo de la Tecnología (PMT)  
c/ Esteve Terradas nº5 - Building C3 - Office 206  
08860 Castelldefels (Barcelona, Spain)

Corresponding author: R. Otin, e-mail: [rotin@cimne.upc.edu](mailto:rotin@cimne.upc.edu)  
tel.: +34 93 413 41 79, fax: +34 93 413 72 42

**Abstract** - In this paper we present a finite element model in frequency domain which computes the Lorentz force that drives an electromagnetic forming (EMF) process. The only input data required are the electrical parameters of the capacitor bank, the coil and the work piece. The main advantage of this approach is that it provides an explicit relation between the parameters of the EMF process and the frequency of the discharge, which is a key parameter in the design of an optimum EMF system. The method is computationally efficient because it only requires to solve time-harmonic Maxwell's equations for a few frequencies and it can be very useful for coil design and for testing modeling conditions on complex three-dimensional geometries.

**Keywords** - Electromagnetism, electromagnetic forming, Lorentz force, numerical analysis, finite element method.

# 1 Introduction

Electromagnetic forming (EMF) is a high velocity forming technique that uses electromagnetic forces to shape metallic work pieces. The process starts when a capacitor bank is discharged through a coil. The transient electric current which flows through the coil generates a time-varying magnetic field around it. By Faraday's law of induction, the time-varying magnetic field induces electric currents in any nearby conductive material. According to Lenz's law, these induced currents flow in the opposite direction to the primary currents in the coil. Then, by Ampère's force law, a repulsive force arises between the coil and the conductive material. If this repulsive force is strong enough to stress the work piece beyond its yield point then it can shape it with the help of a die or a mandrel.

Although low-conductive, non-symmetrical, heavy gauge or small diameter work pieces may not be suitable for EMF, this technique presents several advantages. For example: no tool marks are produced on the surfaces of the work pieces, no lubricant is required, improved formability, less wrinkling, controlled springback, reduced number of operations and lower energy cost. In order to successfully design sophisticated EMF systems and control their performance, it is necessary to advance in the development of theoretical and numerical models of the EMF process. This is the objective of the present work. More specifically, we focus our attention on the numerical analysis of the electromagnetic part of the EMF process. For a review on the state-of-the-art of EMF see [40, 31, 6, 9, 19] or the introductory chapters in [21, 33, 5, 34], where a general overview about the EMF process and also

an abundant bibliography are given.

In this paper we present a method to compute numerically the Lorentz force that drives an EMF process. The input data required are the geometry and material properties of the system *coil-work piece* and the electrical parameters of the capacitor bank. With these data and time-harmonic Maxwell's equations we are able to calculate the current flowing through the coil and the electromagnetic forces acting on the work piece. The main advantage of this method is that it provides an explicit relation between the parameters of the EMF process and the frequency of the discharge, which as it is shown in [13, 43, 11], is a key parameter in the design of optimum EMF systems. The method is computationally efficient because it only requires to solve time-harmonic Maxwell's equations for a few frequencies (around 15 frequency points are usually enough) which, moreover, can be calculated in parallel and independently of one another. With this small amount of simulations we are able to obtain the Lorentz force for all the possible values of the external RLC circuit. Therefore, our frequency domain approach can be very useful for coil design and for testing modeling conditions on complex three-dimensional geometries. Also, it can be used to estimate the optimum frequency and capacitance at which the maximum work piece deformation is attained for a given initial energy and a given set of coil and work piece [26, 29].

EMF is fundamentally an electro-thermo-mechanical process [16]. Different coupling strategies have been proposed to solve numerically this multiphysics problem, but they can be reduced to these three categories: direct or monolithic coupling, sequential coupling and loose coupling. In all of them,

a time domain approach is usually employed.

The direct or monolithic coupling [38, 18] consists in solving the full set of field equations every time step. This approach is the most accurate but it does not take advantage of the different time scales characterizing electromagnetic, mechanical and thermal transients. Moreover, the linear system resulting from the numerical discretization leads to large non-symmetric matrices which are computationally expensive to solve and make this approach unpractical.

In the sequential coupling strategy [9, 22, 42, 34, 11] the EMF process is divided into three sub-problems (electromagnetic, thermal and mechanical) and each field is evolved keeping the others fixed. Usually the EMF process is considered adiabatic and only the numerical solution of the electromagnetic and the mechanical equations are alternately determined. That is, the Lorentz forces are first calculated and then automatically transferred as input load to the mechanical model. The work piece is deformed according to the mechanical model and, thereafter, the geometry of the electromagnetic model is updated and so on. These iterations are repeated until the end of the EMF process. The advantages of this method are that it is very accurate and it can be made computationally efficient.

In the loose coupling strategy [19] the Lorentz forces are calculated neglecting the work piece deformation. Then, they are transferred to the mechanical model which uses them as a driving force to deform the work piece. This approach is less accurate than the former methods, but it is computationally the most efficient and it can be very useful for estimating the order of magnitude of the parameters of an EMF process, for experimentation on

modeling conditions or for modeling complex geometries. Also, it provides results as accurate as the other strategies in processes in which almost all the electromagnetic energy is transferred to the work piece before the changes in the geometrical configuration start to be significant (e.g., in processes with small deformations or abrupt magnetic pressure pulses). In [1, 41, 15] a comparative study of the performance of this approach compared to the sequential coupling strategy is presented.

In this work we perform all electromagnetic computations neglecting the work piece deformation. This is done for clarity reasons and also because the results obtained with a static, un-deformed work piece are useful for a rough estimation of the parameters involved in an EMF process. Moreover, in many situations the usual uncertainties in the knowledge of some EMF parameters can spoil any improvement generated by the computationally more expensive sequential coupling.

The main source of uncertainties in an EMF set-up comes from the mechanical behavior of the work piece at high strain rates and, if present, from its interaction with the die [32]. Mechanical models and its related parameters can be well-known for quasi-static deformations, but are more difficult to obtain and less known for high strain rate deformation processes [10, 31]. Another source of uncertainties are the electrical parameters of the RLC circuit. The electrical properties of the connectors or the junctions between the different parts of the circuit are not always measured properly or taken into account, which difficults the comparison between simulations and measurements (see [21]).

On the other hand, if we have a precise knowledge of all the EMF pa-

rameters and we want to improve the accuracy of the simulations then, we can consider our results as the first step of a sequential coupling strategy. That is, we transfer the force calculated on the un-deformed work piece to the mechanical model. The work piece is deformed according to the mechanical model until it reaches a prefixed amount of deformation. Then, we input the new geometry into the electromagnetic model and so on. In this sequential strategy it is not necessary to solve the electromagnetic equations in each time step. It is only necessary to solve them when the deformation of the work piece produces appreciable changes in the electromagnetic parameters of the system *coil-work piece* (i.e., inductance, resistance, and Lorentz force), which saves computational resources.

## 2 Electromagnetic model

The electromagnetic model taken as a basis in the present work starts by solving time-harmonic Maxwell's equations in a frequency interval. For each frequency  $\omega = 2\pi\nu$  we compute the electromagnetic fields  $\mathbf{E}(\mathbf{r}, \omega)$  and  $\mathbf{H}(\mathbf{r}, \omega)$  inside a volume  $v$  containing the coil and the work piece (system *coil-work piece*). With these fields we compute the inductance  $L_{cw}(\omega)$  and the resistance  $R_{cw}(\omega)$  of the system *coil-work piece*. With  $L_{cw}(\omega)$  and  $R_{cw}(\omega)$  we obtain the intensity  $I(t)$  of the current flowing through the coil. Finally, with  $I(t)$ ,  $\mathbf{E}(\mathbf{r}, \omega)$  and  $\mathbf{H}(\mathbf{r}, \omega)$  we can calculate the Lorentz force that drives the EMF process.

## 2.1 Time-harmonic Maxwell's equations

We start our computations by solving time-harmonic Maxwell's equations inside a volume containing the coil and the work piece. For that purpose, we can use any finite element method (FEM) software in the frequency domain able to provide the fields  $\mathbf{E}(\mathbf{r}, \omega)$  and  $\mathbf{H}(\mathbf{r}, \omega)$  inside the problem domain. In this work, we employ an in-house code called ERMES [25, 7]. This computational tool is the C++ implementation of the FEM formulation explained in [23, 27]. For more details and applications of ERMES see also [24, 30, 28].

The time-harmonic electromagnetic fields  $\mathbf{E}(\mathbf{r}, \omega)$  and  $\mathbf{H}(\mathbf{r}, \omega)$  must be calculated, in theory, for the frequencies  $\omega \in (-\infty, \infty)$ . But, in practice, it is only necessary to solve Maxwell's equations in the interval

$$0 \leq \omega \leq \frac{2}{\mu\sigma (0.4\tau)^2} \quad (1)$$

where  $\mu$  is the magnetic permeability of the work piece,  $\sigma$  is its electrical conductivity and  $\tau$  is the thickness of the work piece. The maximum frequency in (1) is the frequency which makes the skin depth  $\delta = \sqrt{2/\omega\mu\sigma}$  equal to  $\delta = 0.4\tau$ . This value is selected because it has been observed in the literature that, in general, the frequencies used in an EMF discharge accomplish  $\omega_{1.5\tau} \leq \omega \leq \omega_{0.5\tau}$ . Therefore, if we solve time-harmonic Maxwell's equations in the interval (1), we guarantee that all the frequencies of practical interest are covered.

The useful frequencies of an EMF discharge are usually inside the interval  $\omega_{1.5\tau} \leq \omega \leq \omega_{0.5\tau}$  because if the frequency of the triggering current is

too low ( $\omega < \omega_{1.5\tau}$ ) the induced eddy currents are not strong enough to drive a forming process, since their intensity is proportional to the time derivative of the magnetic flux, which in turn is proportional to the slope of the triggering current. This explains why a sufficient high frequency is required for electromagnetic forming. Moreover, at low frequencies, with a skin depth  $\delta > 1.5\tau$ , the magnetic field is permeating in excess of the work piece's thickness, favoring the *magnetic cushion* effect [2, 17]. This effect hinders the deformation of the work piece by generating a magnetic pressure contrary to its movement. On the other hand, if the frequency of the triggering current is too high ( $\omega > \omega_{0.5\tau}$ ) the transmission of momentum from the electromagnetic fields to the work piece is not efficient and the transformation of electromagnetic energy into mechanical deformation is less effective (see [26]). This mainly happens, because the reduced skin depth ( $\delta < 0.5\tau$ ) increases Ohmic losses and hence the field energy is turned into heat instead of plastic deformation.

The interval (1) has been obtained taking into account that the fields  $\mathbf{E}_n(\mathbf{r}, \omega)$  and  $\mathbf{H}_n(\mathbf{r}, \omega)$  (defined in Section 2.5, equations (22) and (23)) are symmetric with respect to the frequency (i.e.,  $\mathbf{E}_n(\mathbf{r}, \omega) = \mathbf{E}_n(\mathbf{r}, -\omega)$  and  $\mathbf{H}_n(\mathbf{r}, \omega) = \mathbf{H}_n(\mathbf{r}, -\omega)$ ), which makes it possible to generate the whole spectrum from the fields computed only in  $\omega \in [0, \infty)$ .

Finally, we have also taken into account that the spectra of the fields possess a sharp peak around the frequency of the discharge  $\omega_0$  (see Section 2.5). This implies that the main contribution to the Fourier transforms of the fields (equations (20) and (21)) comes from the frequencies in the close vicinity of  $\omega_0$  and hence their spectra do not spread outside the interval (1).

## 2.2 Inductance and resistance of the system *coil-work piece*

The repulsive force between the coil and the work piece is a consequence of the time varying current  $I(t)$  generated in the RLC circuit of Fig. 1. To calculate  $I(t)$  we first need the values of the inductance  $L_{cw}$  and the resistance  $R_{cw}$ . We do not take into account the capacitance of the system *coil-work piece* because it is negligible in the geometries and at the frequencies usually involved in electromagnetic forming. The same is applicable to the capacitance of the cables connecting the coil with the capacitor bank.

We consider the set *coil-work piece* as a generic, two-terminal, linear, passive electromagnetic system operating at low frequencies. We can imagine the coil and the work piece inside a volume  $v$  with only its input terminals protruding. Under these assumptions, the inductance  $L_{cw}$  and the resistance  $R_{cw}$  at the frequency  $\omega$  can be calculated with [14, 12]

$$L_{cw}(\omega) = \frac{1}{|I_n|^2} \int_v \mu |\mathbf{H}(\mathbf{r}, \omega)|^2 dv, \quad (2)$$

$$R_{cw}(\omega) = \frac{1}{|I_n|^2} \int_v \sigma |\mathbf{E}(\mathbf{r}, \omega)|^2 dv \quad (3)$$

where  $I_n$  is the current injected into the system through the input terminals,  $\mu$  is the magnetic permeability,  $\mathbf{H}(\mathbf{r}, \omega)$  is the magnetic field,  $\sigma$  is the electrical conductivity and  $\mathbf{E}(\mathbf{r}, \omega)$  is the electric field. Inside the volume of the coil we replace equation (3) by the equation

$$R_{cw}(\omega) = \frac{1}{|I_n|^2} \int_v \frac{|\mathbf{J}(\mathbf{r}, \omega)|^2}{\sigma} dv \quad (4)$$

where  $\mathbf{J}(\mathbf{r}, \omega)$  includes the imposed and induced current densities and  $\sigma$  is the conductivity of the coil.

The injected current  $I_n$  is a dummy variable that is only used to excite the problem. It can take any value without affecting the final result of (2) and (3). We usually impose a spatially constant current density with  $\mathbf{J}_{\text{imp}} = 1 \text{ MA/m}^2$  in the volume of the coil and obtain  $I_n$  from a surface integral of the total current density  $\mathbf{J} = \mathbf{J}_{\text{imp}} + \sigma \mathbf{E}$ .

### 2.3 RLC circuit

In Fig. 1 a typical RLC circuit used in electromagnetic forming is shown. This circuit has a resistance  $R$ , an inductance  $L$  and a capacitance  $C$  given by

$$\begin{aligned} R &= R_{cb} + R_{con} + R_{cw}, \\ L &= L_{cb} + L_{con} + L_{cw}, \\ C &= C_{cb}. \end{aligned} \tag{5}$$

The values of  $R$  and  $L$  vary with time because of the deformation of the work piece. In contrast, the capacitance  $C$  remains constant during the whole forming process. The intensity  $I(t)$  for all  $t \in [0, \infty)$  flowing through the circuit of Fig. 1 satisfies the differential equation

$$0 = \frac{d^2}{dt^2} (LI) + \frac{d}{dt} (RI) + \frac{1}{C}I, \tag{6}$$

with initial conditions  $V(t_0) = V_0$  and  $I(t_0) = 0$ . The initial value  $V_0$  represents the voltage at the terminals of the capacitor. This voltage is

related with the energy of the discharge  $U_0$  by

$$U_0 = \frac{1}{2}CV_0^2. \quad (7)$$

To find  $I(t)$  with (6) we have to know first  $R(t)$  and  $L(t)$  for all  $t \in [0, \infty)$ .

If we consider a loose coupling strategy, the functions  $R(t)$  and  $L(t)$  are constants and equal to the values  $R_0$  and  $L_0$  calculated at the initial position with an un-deformed work piece. Therefore, we have that  $R(t) = R_0$  and  $L(t) = L_0$  for all  $t \in [0, \infty)$ . Under these circumstances, the solution of (6) is given by

$$I(t) = \frac{V_0}{\omega_0 L_0} e^{-\gamma_0 t} \sin(\omega_0 t), \quad (8)$$

where

$$\omega_0 = 2\pi\nu_0 = \sqrt{\frac{1}{L_0 C} - \left(\frac{R_0}{2L_0}\right)^2} \quad (9)$$

and

$$\gamma_0 = \frac{R_0}{2L_0}. \quad (10)$$

If we consider a sequential coupling strategy then we solve (6) in time intervals  $[t_i, t_{i+1}]$ . These time intervals correspond with the time periods between two successive calls to the electromagnetic equations. We can assume that  $L(t)$  and  $R(t)$  are constants inside each  $[t_i, t_{i+1}]$  and equal to the values  $R_i$  and  $L_i$  calculated with the deformed work piece at  $t_i$ . In a sequential coupling strategy, the expression (8) can be considered to be the solution of the first time interval  $[t_0, t_1]$ .

## 2.4 Frequency of the discharge

Equation (8) shows that if we want to know the intensity  $I(t)$  we have to know first the values of  $C$ ,  $V_0$ ,  $L_0$ ,  $R_0$ , and  $\omega_0$ . The capacitance  $C$  and the voltage  $V_0$  are given data, but the inductance  $L_0$ , the resistance  $R_0$  and the frequency  $\omega_0$  must be calculated. This is the objective of this section.

For a given capacitance  $C_{cb}$ , the frequency of the discharge  $\omega_0$  can be found by solving the implicit equation

$$C_0(\omega) - C_{cb} = 0, \quad (11)$$

where  $C_0(\omega)$  is obtained after reordering expression (9) by the relation

$$C_0(\omega) = \frac{4L_0(\omega)}{4\omega^2 L_0(\omega)^2 + R_0(\omega)^2}. \quad (12)$$

Equation (11) can be solved with any root-finding method available (e.g., bisection method or the false position method). In this work, we simply take the result from the graphical representation of  $C_0(\omega)$  (see Fig. 14).

The functions  $L_0(\omega)$  and  $R_0(\omega)$  appearing in (12) are obtained with the help of equations (2)-(5). We must take into account that the intensity (8) is an exponentially decaying sinusoid with a frequency spectrum given by (25). Therefore, we must average  $L_0(\omega)$  and  $R_0(\omega)$  over this spectrum

$$\langle L_0(\omega) \rangle = \int L_0(\omega') F_\omega(\omega') d\omega', \quad (13)$$

$$\langle R_0(\omega) \rangle = \int R_0(\omega') F_\omega(\omega') d\omega', \quad (14)$$

where  $F_\omega$  is the normalized spectrum of the intensity (8) oscillating at the frequency  $\omega$ . The problem is that, to obtain the spectrum of (8), we must know first the values of  $L_0$  and  $R_0$  for the frequency of an oscillation which is not damped (see equation (25)). This circular loop can be broken using an iterative procedure. That is, for a given frequency  $\omega$ , we introduce the values of  $L_0 = L_0(\omega)$  and  $R_0 = R_0(\omega)$  in  $F_\omega$ . Then, with this  $F_\omega$ , we calculate  $\langle L_0(\omega) \rangle$  and  $\langle R_0(\omega) \rangle$  with (13) and (14). These averaged values are introduced in  $F_\omega$  and, then, a new average is computed. This process will continue until the values of  $\langle L_0(\omega) \rangle$  and  $\langle R_0(\omega) \rangle$  stop changing (up to a previously determined tolerance).

Fortunately, the above calculations can be simplified thanks to the sharply peaked shape of  $F_\omega$  around the frequency of the discharge and the slow variation of the functions  $L_0(\omega)$  and  $R_0(\omega)$  along the frequencies of practical interest (see Sections 2.1 and 3 and the examples in [26]). These two circumstances make  $\langle L_0(\omega) \rangle \approx L_0(\omega)$  and  $\langle R_0(\omega) \rangle \approx R_0(\omega)$  to be a good approximation. Even for lower frequencies, where the variations of  $L_0(\omega)$  and  $R_0(\omega)$  with respect to frequency are stronger, this approximation can give good results. For instance, in the examples of [26], it is shown that the low frequency intensities calculated with the above approximation are similar to those measured or calculated with other numerical methods.

For the above reasons, in this work, we consider that the behavior of the inductance and resistance of the RLC circuit with respect to the frequency satisfies  $\langle L_0(\omega) \rangle = L_0(\omega)$  and  $\langle R_0(\omega) \rangle = R_0(\omega)$ , being  $L_0(\omega)$  and  $R_0(\omega)$  the functions obtained with (2)-(5). It is also worth to mention that, although the calculation of the current will be more involved if we consider the multi-

frequency nature of  $L$  and  $R$ , the computational efficiency of the method will remain the same, since the number of time-harmonic simulations (the more computational expensive part) is not altered by this fact.

In the case of using a sequential coupling strategy, we must take into account that the functions  $L_i(\omega)$  and  $R_i(\omega)$  are different at each  $[t_i, t_{i+1}]$  and, as a consequence, the frequency  $\omega_i$  is also different at each time interval. Therefore, we must re-calculate  $L_i(\omega)$ ,  $R_i(\omega)$  and  $\omega_i$  every time we call the electromagnetic model.

For a given set of coil, work piece and connectors, the frequency of the discharge is determined by the capacitance  $C_{cb}$ . Usually, the value of  $C_{cb}$  can be selected from a discrete set of capacitances offered by the capacitor bank. Therefore, we can change the frequency of discharge by selecting different values of  $C_{cb}$ . Equivalently, if we want the current intensity to oscillate at a given frequency (for instance, if we know beforehand the optimum frequency of the discharge) then we only need to select  $C_{cb}$  with the help of expression (12).

## 2.5 Lorentz force on the work piece

If we consider that the dimensions of the system *coil-work piece* are small compared with the wavelength of the prescribed fields (quasi-static regime), the materials are linear and the modulus of the velocity at any point is always much less than  $10^7$  m/s then, the Lorentz force per unit volume  $\mathbf{f}(\mathbf{r}, t)$  can be expressed as [37, 20, 21]

$$\mathbf{f}(\mathbf{r}, t) = \mathbf{J}(\mathbf{r}, t) \times \mathbf{B}(\mathbf{r}, t) = \sigma\mu (\mathbf{E}(\mathbf{r}, t) \times \mathbf{H}(\mathbf{r}, t)), \quad (15)$$

where  $\mathbf{r}$  is a point inside the work piece,  $\mathbf{J} = \sigma\mathbf{E}$  is the induced current density and  $\mathbf{B} = \mu\mathbf{H}$  is the magnetic flux density. The above assumptions are effectively accomplished in any EMF system. The frequencies involved in EMF are in the order of  $\nu \approx 10^3 - 10^4$  Hz with wavelengths in the order of  $\lambda \approx 10^3 - 10^5$  m. As a consequence, we can consider the displacement current negligible  $\partial\mathbf{D}/\partial t \approx 0$  (then  $\nabla \cdot \mathbf{J} \approx 0$  and  $\rho \approx 0$ ) and treat the fields as if they propagated instantaneously with no appreciable radiation [37]. Also, the velocities involved in EMF are in the order of  $|\mathbf{v}| \approx 10^2 - 10^3$  m/s, which allows us to neglect the velocity terms that appear in Maxwell's equations when working with moving media [20].

If the work piece is linear, homogeneous and non-magnetic ( $\mu = \mu_0$ ) then we can represent the electromagnetic force as a magnetic pressure

$$P(\mathbf{r}_0, t) = \frac{1}{2} \mu_0 \left( |\mathbf{H}(\mathbf{r}_0, t)|^2 - |\mathbf{H}(\mathbf{r}_\tau, t)|^2 \right), \quad (16)$$

where  $\mathbf{r}_0$  is a point located on the work piece surface facing the coil and  $\mathbf{r}_\tau$  is a point located on its opposite side, perpendicular to  $\mathbf{r}_0$ . To reach this expression we have to remind that, under the assumptions postulated at the beginning of this section, equation (15) can also be expressed as

$$\mathbf{f} = -\nabla \left( \frac{1}{2\mu_0} |\mathbf{B}|^2 \right) + \frac{1}{\mu_0} (\mathbf{B} \cdot \nabla) \mathbf{B}. \quad (17)$$

This equation (17) is obtained from the Lorentz force (15) with the help of

the vector identity

$$\mathbf{B} \times \nabla \times \mathbf{B} = \nabla \left( \frac{1}{2} |\mathbf{B}|^2 \right) - (\mathbf{B} \cdot \nabla) \mathbf{B} \quad (18)$$

and the Ampère's circuital law

$$\nabla \times \mathbf{B} = \mu_0 \mathbf{J}. \quad (19)$$

In EMF the last term of the right hand side of (17) is usually negligible compared with the first. This is equivalent to neglect the compressive and expansive forces parallel to the work piece surface and to state that, in EMF, the electromagnetic forces are due to the change in magnitude of the magnetic field along the thickness of the work piece. If we integrate the first term of (17) along a straight line perpendicular to the work piece surfaces (through its thickness) from the point  $\mathbf{r}_0$  to the point  $\mathbf{r}_\tau$  then we obtain the magnetic pressure (16).

If only linear materials in the system *coil-work piece* are present, then the fields behave linearly with respect to the current intensity (i.e., if we multiply the intensity by a constant then the values of the fields obtained with the new excitation will be also multiplied by the same constant). This implies that  $\mathbf{E}(\mathbf{r}, t)$  and  $\mathbf{H}(\mathbf{r}, t)$  in (15) are related with the fields  $\mathbf{E}(\mathbf{r}, \omega)$  and  $\mathbf{H}(\mathbf{r}, \omega)$  calculated in Section 2.1 by means of the inverse Fourier transform

$$\mathbf{E}(\mathbf{r}, t) = \frac{1}{2\pi} \int_{-\infty}^{\infty} \mathbf{E}_n(\mathbf{r}, \omega) I(\omega) e^{i\omega t} d\omega, \quad (20)$$

$$\mathbf{H}(\mathbf{r}, t) = \frac{1}{2\pi} \int_{-\infty}^{\infty} \mathbf{H}_n(\mathbf{r}, \omega) I(\omega) e^{i\omega t} d\omega, \quad (21)$$

where  $i = \sqrt{-1}$  is the imaginary unit,  $\mathbf{E}_n(\mathbf{r}, \omega)$  and  $\mathbf{H}_n(\mathbf{r}, \omega)$  are the fields per unit intensity at the frequency  $\omega$ , and  $I(\omega)$  is the Fourier transform of the intensity  $I(t)$  flowing through the RLC circuit. The fields per unit intensity are defined by

$$\mathbf{E}_n(\mathbf{r}, \omega) = \frac{\mathbf{E}(\mathbf{r}, \omega)}{I_n}, \quad (22)$$

$$\mathbf{H}_n(\mathbf{r}, \omega) = \frac{\mathbf{H}(\mathbf{r}, \omega)}{I_n}, \quad (23)$$

with  $\mathbf{E}(\mathbf{r}, \omega)$ ,  $\mathbf{H}(\mathbf{r}, \omega)$  and  $I_n$  the fields and intensity appearing in (3) and (2). The advantage of using  $\mathbf{E}_n(\mathbf{r}, \omega)$  and  $\mathbf{H}_n(\mathbf{r}, \omega)$  is that we can determine the fields inside the system *coil-work piece* for any value of the current intensity  $I(\omega)$  once it is known for  $I_n$ . The Fourier transform  $I(\omega)$  is defined as

$$I(\omega) = \int_{-\infty}^{\infty} I(t) e^{-i\omega t} dt. \quad (24)$$

If the intensity  $I(t)$  is given by (8) then the analytical expression of  $I(\omega)$  is

$$I(\omega) = \left( \frac{V_0}{\omega_0 L_0} \right) \frac{1}{2} \left( \frac{1}{\omega + \omega_0 - i\gamma_0} - \frac{1}{\omega - \omega_0 - i\gamma_0} \right), \quad (25)$$

where  $V_0$ ,  $\omega_0$ ,  $L_0$ , and  $\gamma_0$  are the parameters defined in Section 2.3.

In summary, once we know the intensity  $I(t)$  flowing through the coil, we compute its Fourier transform with (24). Then, with (20) and (21), we obtain the fields  $\mathbf{E}(\mathbf{r}, t)$  and  $\mathbf{H}(\mathbf{r}, t)$  required in the Lorentz force expression

(15) or, if applicable, in the magnetic pressure equation (16).

### 3 Application example: Sheet bulging.

To validate the electromagnetic model explained above we will apply it to the EMF process presented in [39]. This process consists in the free bulging of a thin metal sheet by a spiral flat coil. Our objective is to find the Lorentz force acting on the work piece for the given value of the capacitance  $C_{cb} = 40 \mu\text{F}$  and the initial voltage  $V_0 = 6 \text{ kV}$ .

We have selected this example because it is a very well documented benchmark which has been solved by several authors. Moreover, most of the examples shown in the literature present a similar pancake coil setup. Other benchmarks, also widely treated in the literature, are the tube compression and tube expansion, to which we had also applied the method explained here (see [26]).

Although in this example we are solving a simple axisymmetric geometry, the main characteristic of the finite element method is that it can deal easily with complicated geometries and materials. Obviously, we will require more computational resources as the problem gets more complex and bigger. But, as it is mentioned above, we need only a few simulations and these simulations can be solved simultaneously and independently. This paves the path to the implementation of efficient algorithms. Moreover, the electromagnetic fields in the system *coil-work piece* can be calculated with any available finite element code in frequency domain. We used the in-house code ERMES, but more efficient FEM software packages are available in the

market and they can speed-up the computations. The computational performance of ERMES when applied to more complex geometries is shown in [27, 24, 30, 28].

### 3.1 Description of the system *coil-work piece*

The spiral flat coil appearing in [39] can be approximated by coaxial loop currents in a plane. Thus, the problem can be considered axisymmetric. The dimensions of the coil and the work piece are shown in Fig. 2. The diameter of the wire, material properties and horizontal positioning of the coil are missed in [39]. We used the values given in [9], where the same problem is treated and a complete description of the geometry is provided.

The coil is made of copper with electrical conductivity  $\sigma = 58 \times 10^6$  S/m. The work piece is a circular plate of annealed aluminum JIS A 1050 with an electrical conductivity of  $\sigma = 36 \times 10^6$  S/m. It is assumed  $\mu = \mu_0$  in the coil and in the work piece.

The RLC circuit has an inductance  $L_{cb} + L_{con} = 2.0 \mu\text{H}$ , a resistance  $R_{cb} + R_{con} = 25.5 \text{ m}\Omega$  and a capacitance  $C_{cb} = 40 \mu\text{F}$ . The capacitor bank was initially charged with a voltage of  $V_0 = 6 \text{ kV}$ .

### 3.2 Electromagnetic fields in frequency domain

Although, in this case, the optimal choice would be to perform the computations with an axisymmetric two-dimensional computational tool, we used, instead, the full-wave three-dimensional code ERMES. The main advantages of using ERMES are that it is at-hand, it can be customized to our needs and it can solve more general problems.

The FEM model employed is shown in Fig. 3. The geometry is a truncated portion of a sphere with an angle of  $20^\circ$ . We excite the problem with an axisymmetric current density  $\mathbf{J}$  uniformly distributed in the volume of the coil wires. In the colored surfaces of Fig. 3 we imposed a perfect electric conductor (PEC) boundary conditions. It is not necessary to impose more boundary condition if we apply in all the FEM nodes of the domain a change of coordinates from Cartesian  $(E_x, E_y, E_z)$  to axisymmetric around the Y axis  $(E_\rho, E_\varphi, E_y)$ . That is, at the same time as we are building the matrix, we enforce at each node of the FEM mesh

$$\begin{pmatrix} E_\rho \\ E_\varphi \\ E_y \end{pmatrix} = \begin{pmatrix} x/\rho & 0 & z/\rho \\ -z/\rho & 0 & x/\rho \\ 0 & 1 & 0 \end{pmatrix} \begin{pmatrix} E_x \\ E_y \\ E_z \end{pmatrix} \quad (26)$$

where  $x$  and  $z$  are the Cartesian coordinates of the node and  $\rho = \sqrt{x^2 + z^2}$ . We preserve the symmetry of the final FEM matrix applying (26) and its transpose as it is explained in [3]. The advantage of using (26) is that  $E_\rho = 0$  and  $E_y = 0$  in axisymmetric problems. This fact reduces the size of the final matrix and the time required to solve it by a factor of three. Therefore, we can improve noticeably the computational performance of ERMES in axisymmetric problems with a simple modification of its matrix building procedure.

The FEM mesh employed is shown in Fig. 4. It consists of 529189 second order isoparametric nodal finite elements. The fields  $\mathbf{E}(\mathbf{r}, \omega)$  and  $\mathbf{H}(\mathbf{r}, \omega)$  were computed for the frequencies  $\nu = \omega/2\pi \in [0, 40]$  kHz ( $\delta = 0.42\tau$ , see

Section 2.1) with a frequency step of  $\Delta\nu = 1$  Hz. In a desktop computer with a CPU Intel Core 2 Quad Q9300 at 2.5 GHz and the operative system Microsoft Windows XP, ERMES requires around 90 s and 1.5 GB of memory RAM to solve the FEM linear system at each frequency. We employed fine FEM meshes and small frequency steps to guarantee accurate solutions despite the increase in the computational cost. The objective of this paper is to validate our approach and, as a consequence, we put more emphasis in the accuracy of the solutions than in the computational performance.

In Figures 5 to 11 we show the results of the computations for different frequencies. One can see how the fields tend to concentrate in the space between the coil and the work piece and in the surface of the conductors as the frequency increases. This fact raises the resistance  $R_{cw}$  of the system *coil-work piece* (skin effect) and reduces its inductance  $L_{cw}$ , as it is shown in Figures 12 and 13. In Fig. 11 we can see that it is possible to simulate the fields for only a small amount of frequencies in the interval of interest and obtain the rest of the frequencies by a linear combination of the fields yet calculated. Therefore, we can characterize an EMF system electromagnetically after solving time-harmonic Maxwell's equations for only a few frequencies.

### 3.3 Current intensity in the coil

The current intensity in the coil is given by expression (8). The frequency of the discharge is obtained with equations (11) and (12) using the inductance and the resistance calculated as explained in Section 2.4 (see also Figures 12 and 13). In Fig. 14 the capacity  $C_0(\omega)$  of the oscillating circuit is displayed as a function of the frequency according to equation (12), and the frequency

corresponding to a capacitance of  $C_{cb} = 40 \mu\text{F}$  is highlighted. In Fig. 15 the intensity calculated in this work is compared with the intensity simulated by Takatsu et al. [39]. We can observe a good correlation between the numerical values computed for the intensity by both methods, even despite the fact that, in [39], the current intensity is computed with a numerical model in which the work piece deformation is taken into account.

In [39] the mutual inductance between coil and work piece is determined numerically every time step based on computation of the current intensities flowing through coil and work piece. Once these intensities are known, the electromagnetic fields are obtained with a closed analytical solution for loop currents. These fields are imposed as a magnetic pressure in a simulation code which predicts the dynamical behavior of the work piece loaded by impulsive forces. After a small time interval, the inductances are calculated again and so on.

### 3.4 Lorentz force acting on the work piece

We compute the force acting on the work piece with the equations described in Section 2.5 and the fields shown in Section 3.2. In Fig. 16 the total force calculated in this work is compared with that simulated in [39].

In Figures 17 and 18 we show the radial component  $B_\rho$  and the axial component  $B_y$  of the magnetic flux density on the work piece surface facing the coil when the current  $I(t)$  reaches its first maximum. We compare the fields calculated in this work with those simulated by Siddiqui et al. [35, 34].

The EMF process described in this section is simulated in [35, 34] using two different approaches. One is based on FDTD (Finite Difference Time

Domain) and the other on FEM (Finite Element Method). In the FDTD approach, Siddiqui et al. solve Maxwell's equations in time domain with an in-house code. The electromagnetic fields are generated by a pre-calculated current intensity flowing through the coil. This current is a damped sinusoid which is determined neglecting the work piece deformation. On the other hand, in the FEM approach, Siddiqui et al. solve time-harmonic Maxwell's equations with the freeware software FEMM4.0 [8]. In [34], the fields are calculated with FEMM4.0 assuming a time-harmonic current intensity oscillating at a frequency and with a maximum value equal to the first pulse of the current intensity simulated in [39].

We can see in Figures 17 and 18 that (apart from a shift caused by using a different positioning of the coil) the results given by both FEM codes are similar to each other, but different from the results given by the FDTD method. The differences between the FDTD and the FEM approaches can be attributed to the use of a coarse mesh in the FDTD method. To show this, we solved a problem similar to the one described here but with a fixed work piece of thickness  $\tau = 3.0$  mm, gap distance  $h = 2.9$  mm and initial voltage  $V_0 = 2$  kV. We calculated in this set-up the radial component of the magnetic flux density  $B_\rho$ . Then, we compared our results with the simulations performed in [34] for different FDTD mesh sizes. In Fig. 19 we see that when the FDTD mesh is coarse (6 elements along the thickness of the sheet) the results of the FDTD simulations are different from the results obtained with ERMES. If we improve the FDTD mesh to 20 elements along the thickness of the sheet, the results of the FDTD simulations are similar to the results obtained with ERMES. Therefore, it is clear that we need a

fine mesh in the work piece to simulate properly the electromagnetic fields.

### 3.5 Deformation of the work piece

For comparative purposes we also calculated the deformation of the work piece. The mechanical equations were solved with the commercial software STAMPAK [36]. This numerical tool has been applied to processes such as ironing, necking, embossing, stretch-forming, forming of thick sheets, flex-forming, hydro-forming, stretch-bending of profiles, etc. It can solve dynamic problems with high speeds and large strain rates, obtaining explicitly accelerations, velocities and deformations. In this work, our emphasis is on the electromagnetic part of the EMF process, hence, we do not go further into the numerical formulation behind STAMPAK. For a detailed information about this formulation see [4].

We introduced in STAMPAK the magnetic pressure calculated with the fields of Section 3.4 and the equation (16). STAMPAK interprets this magnetic pressure as a mechanical pressure which deforms the work piece. The results are shown in Fig. 20.

In STAMPAK the mechanical model used in [39] is not available. Therefore, we had to adapt the parameters of the available model to reproduce the behavior of the material used in [39]. We considered the work piece as an aluminium alloy with a Young's modulus equal to 69 GPa, mass density of 2700 kg/m<sup>3</sup> and Poisson's ratio equal to 0.33. STAMPAK used the Voce hardening law

$$\sigma_{cs} = \sigma_{y0} + (\sigma_m - \sigma_{y0}) (1 - e^{-n\varepsilon_{ps}}), \quad (27)$$

where  $\sigma_{cs}$  is the Cauchy stress,  $\sigma_{y0} = 34.9 \text{ MPa}$  is the yielding tensile strength,  $\sigma_m = 128.8 \text{ MPa}$  is the ultimate tensile strength,  $n = 12.0$  is the isotropic hardening parameter and  $\varepsilon_{ps}$  is the effective plastic deformation. STAMPAK also used a damping proportional to the nodal velocity ( $\mathbf{F}_i = -\eta_i \mathbf{v}_i$ ) with  $\eta_i = 2\alpha M_i$ , being  $\alpha = 138.6 \text{ s}^{-1}$  and  $M_i$  the lumped mass at the  $i$ -th node. The constant parameters of the mechanical model were obtained introducing in STAMPAK the magnetic pressure simulated in [39]. Then, we adjusted the parameters until we achieved with STAMPAK the same deformation of the disk as measured in [39]. The parameters were calculated in this way because the objective of the mechanical simulation was to compare the behavior of the work piece under the magnetic pressure simulated by Takatsu et al. and the one calculated in this work.

As can be observed from the deformation of the work piece measured by Takatsu et al. (see Fig. 20) the movement of the work piece starts when the decreasing part of the first half wave of the strongly damped discharging pulse is almost over and, hence, nearly all energy of the electromagnetic field is already transferred to the work piece (see Fig. 16). This explains, why in this case, it is a good approximation to neglect the work piece deformation.

## 4 Conclusion

In this paper we have presented a numerical model for the simulation of the electromagnetic forming processes. This method is computationally efficient because it only requires to solve time-harmonic Maxwell's equations for a few frequencies to have completely characterized the EMF system. Once

we know the fields inside a volume containing the coil and the work piece, we can easily calculate the Lorentz forces that drives the EMF process for all the possible variations of the external circuit (e.g., we do not need to repeat the simulations if the capacitance  $C_{cb}$  is changed). The approach can be very useful for coil design, estimating the order of magnitude of the parameters of an EMF process, for experimentation on modeling conditions or for modeling complex three-dimensional geometries. Moreover, it can be easily included in a sequential coupling strategy if higher precision is required. Also, it offers an alternative to the more extended time domain methods and a new insight into the physics of EMF.

## Acknowledgment

The work described in this paper and the research leading to these results has received funding from the Spanish Ministry of Education and Science through the National R+D Plan 2004-2007, reference DPI2006-15677-C02-01, SICEM project.

## References

- [1] G. Bartels, W. Schaetzing, H.-P. Scheibe, and M. Leone. Simulation models of the electromagnetic forming process. *Acta Physica Polonica A*, 115:1128–1129, 2009.
- [2] I. V. Belyy, S. M. Fertik, and L. T. Khimenko. *Electromagnetic Metal Forming Handbook*. Translation by M. M. Al-

tynova and G. S. Daehn of the Russian book: Spravochnik po Magnitno-Impul'snoy Obrabotke Metallov. Available On-line: [www.matsceng.ohio-state.edu/~daehn/metalforminghb](http://www.matsceng.ohio-state.edu/~daehn/metalforminghb), 1996.

- [3] W. E. Boyse, D. R. Lynch, K. D. Paulsen, and G. N. Minerbo. Nodal-based finite-element modeling of Maxwell's equations. *IEEE Transactions on Antennas and Propagation*, 40:642–651, 1992.
- [4] P. Cendoya, E. Oñate, and J. Miquel. Nuevos elementos finitos para el análisis dinámico elastoplástico no lineal de estructuras laminares. Technical report, International Center for Numerical Methods in Engineering (CIMNE), ref.: M-36, 1997.
- [5] M. S. Dehra. *High Velocity Formability And Factors Affecting It*. PhD thesis, The Ohio State University, 2006.
- [6] A. El-Azab, M. Garnich, and A. Kapoor. Modeling of the electromagnetic forming of sheet metals: state-of-the-art and future needs. *Journal of Materials Processing Technology*, 142:744–754, 2003.
- [7] ERMES. A finite element code for electromagnetic simulations in frequency domain. R. Otin, CIMNE, Barcelona, Spain. [Online]. Available: <https://web.cimne.upc.edu/users/rotin/web/software.htm>, [http://cpc.cs.qub.ac.uk/summaries/AEPV\\_v1\\_0.html](http://cpc.cs.qub.ac.uk/summaries/AEPV_v1_0.html), 2013.
- [8] FEMM. Finite element method magnetics. David Meeker, USA. [Online]. Available: <http://www.femm.info/wiki/HomePage>, 2010.

- [9] G. K. Fenton and G. S. Daehn. Modelling of the electromagnetically formed sheet metal. *Journal of Materials Processing Technology*, 75:6–16, 1998.
- [10] J.E. Field, S.M. Walley, W.G. Proud, H.T. Goldrein, and C.R. Siviour. Review of experimental techniques for high rate deformation and shock studies. *International Journal of Impact Engineering*, 30(7):725–775, 2004.
- [11] Y. U. Haiping and L. I. Chunfeng. Effects of current frequency on electromagnetic tube compression. *Journal of Materials Processing Technology*, 209:1053–1059, 2009.
- [12] Chang-Hwan Im and Hyun-Kyo Jung. Numerical computation of inductance of complex coil systems. *International Journal of Applied Electromagnetics and Mechanics*, 29(1):15–23, 2009.
- [13] J. Jablonski and R. Winkler. Analysis of the electromagnetic forming process. *International Journal of Mechanical Sciences*, 20:315–325, 1978.
- [14] J. D. Jackson. *Classical Electrodynamics*. John Wiley & Sons, Inc., 3rd edition, 1999.
- [15] M. Kleiner, A. Brosius, H. Blum, F.-T. Suttmeier, M. Stiemer, B. Svendsen, J. Unger, and S. Reese. Benchmark simulation for coupled electromagnetic-mechanical metal forming processes. *Production Engineering and Development*, 11:85–90, 2004.

- [16] Chia-Lung Kuo, Jr-Shiang You, and Shun-Fa Hwang. Temperature effect on electromagnetic forming process by finite element analysis. *International Journal of Applied Electromagnetics and Mechanics*, 35(1):25–37, 2011.
- [17] A. G. Mamalis, A. G. Kladas, A. K. Koumoutsos, and D. E. Manolakos. Electromagnetic forming and powder processing: trends and developments. *Applied Mechanics Reviews*, 57(4):299–324, 2004.
- [18] A. G. Mamalis, D. E. Manolakos, A. G. Kladas, and A. K. Koumoutsos. Physical principles of electromagnetic forming process: a constitutive finite element model. *Journal of Materials Processing Technology*, 161:294–299, 2005.
- [19] A. G. Mamalis, D. E. Manolakos, A. G. Kladas, and A. K. Koumoutsos. Electromagnetic forming tools and processing conditions: numerical simulation. *Materials and Manufacturing Processes*, 21:411–423, 2006.
- [20] T. E. Manea, M. D. Verweij, and H. Blok. The importance of the velocity term in the electromagnetic forming process. *The 27th General Assembly of the International Union of Radio Science (URSI 2002)*, Maastricht, The Netherlands, 17-24 August, 2002.
- [21] T. E. Motoasca. *Electrodynamics in Deformable Solids for Electromagnetic Forming*. PhD thesis, Delft University of Technology, 2003.
- [22] D.A. Oliveira, M.J. Worswick, M. Finn, and D. Newmanc. Electromagnetic forming of aluminum alloy sheet: Free-form and cavity fill

- experiments and model. *Journal of Materials Processing Technology*, 170:350–362, 2005.
- [23] R. Otin. Regularized Maxwell equations and nodal finite elements for electromagnetic field computations. *Electromagnetics*, 30(1-2):190–204, 2010.
- [24] R. Otin. Numerical study of the thermal effects induced by a RFID antenna in vials of blood plasma. *Progress In Electromagnetics Research Letters*, 22:129–138, 2011.
- [25] R. Otin. ERMES: A nodal-based finite element code for electromagnetic simulations in frequency domain. *Computer Physics Communications*, 184(11):2588–2595, 2013.
- [26] R. Otin. A numerical model for the search of the optimum frequency in electromagnetic metal forming. *International Journal of Solids and Structures*, 50(10):1605–1612, 2013.
- [27] R. Otin, L. E. Garcia-Castillo, I. Martinez-Fernandez, and D. Garcia-Doñoro. Computational performance of a weighted regularized Maxwell equation finite element formulation. *Progress In Electromagnetics Research*, 136:61–77, 2013.
- [28] R. Otin and H. Gromat. Specific absorption rate computations with a nodal-based finite element formulation. *Progress In Electromagnetics Research*, 128:399–418, 2012.

- [29] R. Otin, R. Mendez, and O. Frutos. A numerical model for the search of the optimum capacitance in electromagnetic metal forming. *The 8th International Conference and Workshop on Numerical Simulation of 3D Sheet Metal Forming Processes (NUMISHEET 2011), August 21-26, Seoul (Korea), 2011.*
- [30] R. Otin, J. Verpoorte, and H. Schippers. A finite element model for the computation of the transfer impedance of cable shields. *IEEE Transactions On Electromagnetic Compatibility*, 53(4):950–958, 2011.
- [31] V. Psyk, D. Risch, B.L. Kinsey, A.E. Tekkaya, and M. Kleiner. Electromagnetic forming-A review. *Journal of Materials Processing Technology*, 211(5):787–829, 2011.
- [32] D. Risch, C. Beerwald, A. Brosius, and M. Kleiner. On the significance of the die design for electromagnetic sheet metal forming. *The 1st International Conference on High Speed Forming (ICHSF2004), Dortmund (Germany), March 31-April 4, 2004.*
- [33] J. Shang. *Electromagnetically Assisted Sheet Metal Stamping*. PhD thesis, The Ohio State University, 2006.
- [34] M. A. Siddiqui. *Numerical Modelling And Simulation Of Electromagnetic Forming Process*. PhD thesis, University of Strasbourg, 2009.
- [35] M. A. Siddiqui, J. P. M. Correia, S. Ahzi, and S. Belouettar. A numerical model to simulate electromagnetic sheet metal forming process. *International Journal of Material Forming*, 1:1387–1390, 2008.

- [36] STAMPACK. A general finite element system for sheet stamping and forming problems. *Quantech ATZ, Barcelona, Spain*. [Online]. Available: <http://www.quantech.es>, 2010.
- [37] J. A. Stratton. *Electromagnetic Theory*. McGraw-Hill, 1941.
- [38] B. Svendsen and T. Chanda. Continuum thermodynamic formulation of models for electromagnetic thermoelastic solids with application in electromagnetic metal forming. *Continuum Mechanics and Thermodynamics*, 17:1–16, 2005.
- [39] N. Takatsu, M. Kato, K. Sato, and T. Tobe. High-speed forming of metal sheets by electromagnetic force. *The Japan Society of Mechanical Engineers International Journal*, 31:142–148, 1988.
- [40] A.E. Tekkaya, G.S. Daehn, and M. Kleiner. High speed forming 2012. *Proceedings of the 5th international conference on high speed forming (ICHSF2012), April 24-26, Dortmund (Germany)*, 2012.
- [41] I. Ulacia, I. Hurtado, J. Imbert, M. J. Worswick, and P. L’Eplattenier. Influence of the coupling strategy in the numerical simulation of electromagnetic sheet metal forming. *The 10th International LS-DYNA Users Conference, Dearborn, Michigan USA, June 8-10*, 2008.
- [42] J. Unger, M. Stiemer, M. Schwarze, B. Svendsen, H. Blum, and S. Reese. Strategies for 3D simulation of electromagnetic forming processes. *Journal of Materials Processing Technology*, 199:341–362, 2008.

- [43] H. Zhang, M. Murata, and H. Suzuki. Effects of various working conditions on tube bulging by electromagnetic forming. *Journal of Materials Processing Technology*, 48:113–121, 1995.

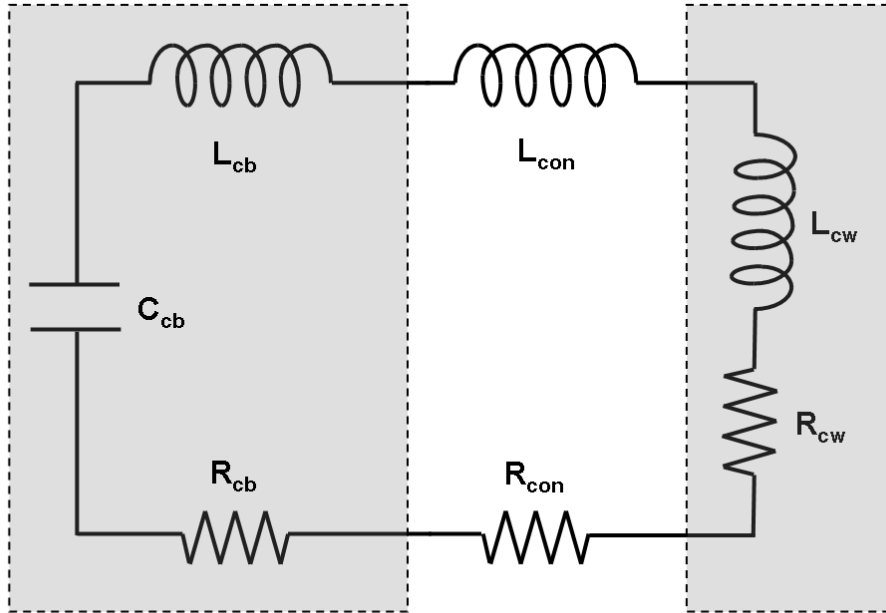


Figure 1: RLC circuit used to produce the discharge current. In the shadowed rectangle on the left the capacitor bank with capacitance  $C_{cb}$ , inductance  $L_{cb}$  and resistance  $R_{cb}$  is represented. In the shadowed rectangle on the right the system formed by the coil and the metal work piece is represented. This system has an inductance  $L_{cw}$  and a resistance  $R_{cw}$ . Between both rectangles the cables connecting the capacitor bank with the coil are represented. These cables have an inductance  $L_{con}$  and a resistance  $R_{con}$ .

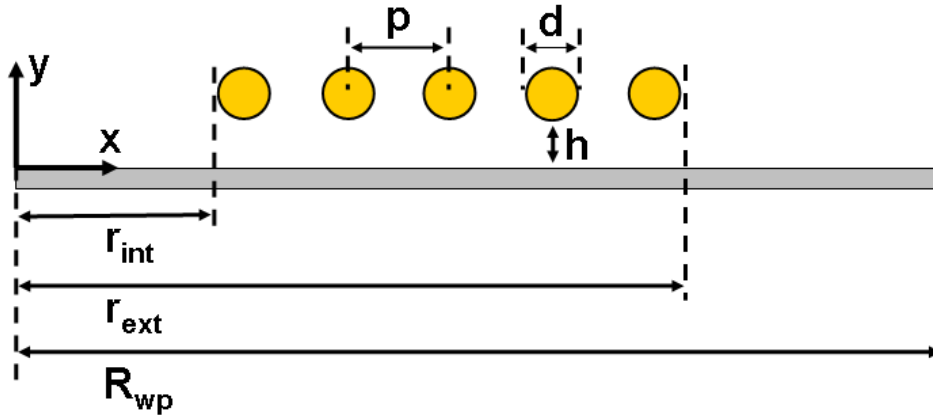


Figure 2: Dimensions of the system *coil-work piece*, data taken from [39, 9]: number of turns of the coil  $N = 5$ , pitch or distance between two neighboring turns  $p = 5.5$  mm, diameter of the coil wires  $d = 1.29$  mm (16 AWG), maximum coil radius  $r_{ext} = 32$  mm, minimum coil radius  $r_{int} = 8.71$  mm, distance between coil and metal sheet  $h = 1.6$  mm, thickness of the sheet  $\tau = 0.5$  mm, radius of the work piece  $R_{wp} = 55$  mm.

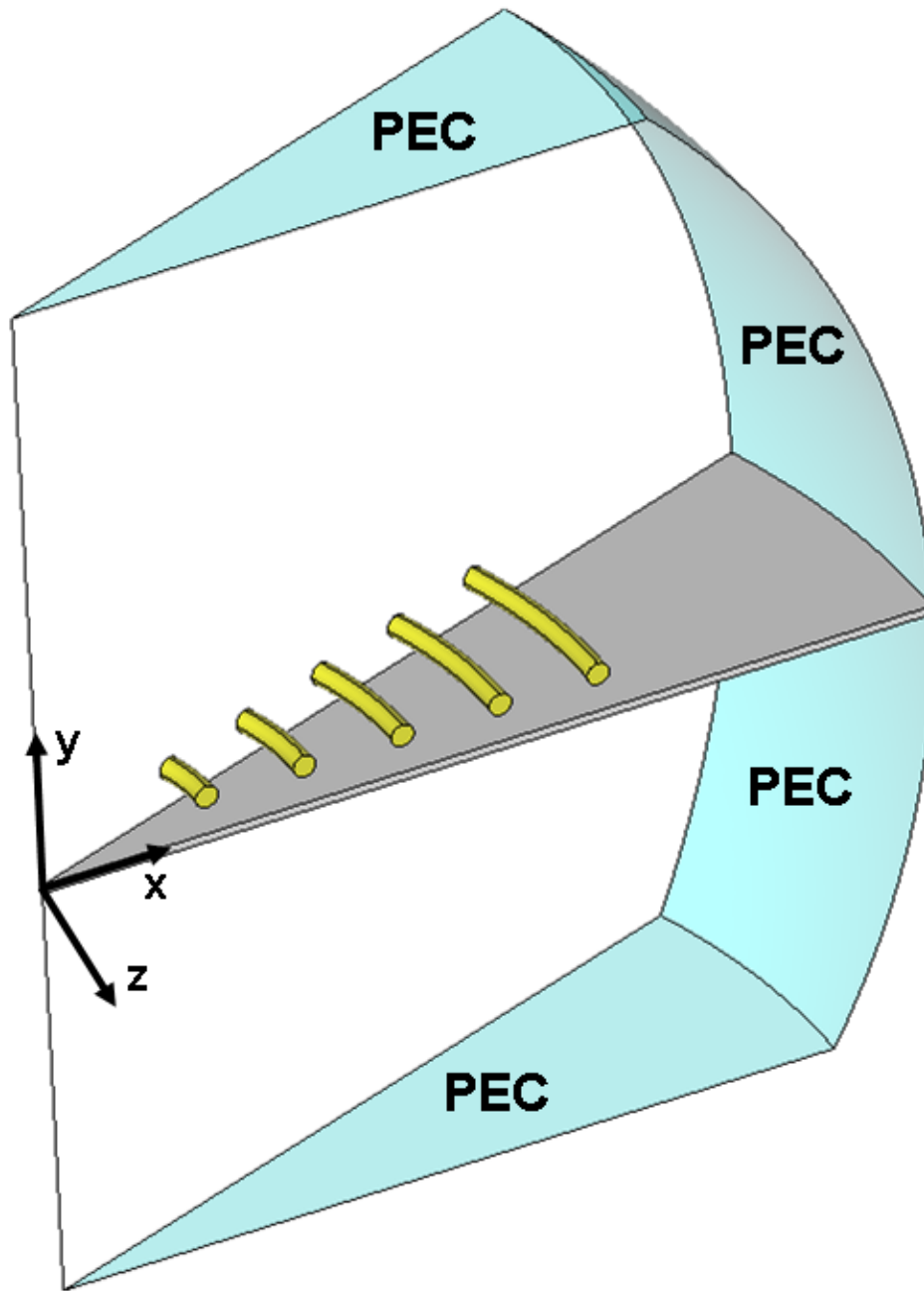


Figure 3: CAD geometry used in ERMES to compute the time-harmonic electromagnetic fields. In the blue colored surfaces a perfect electric conductor (PEC) boundary condition was applied.

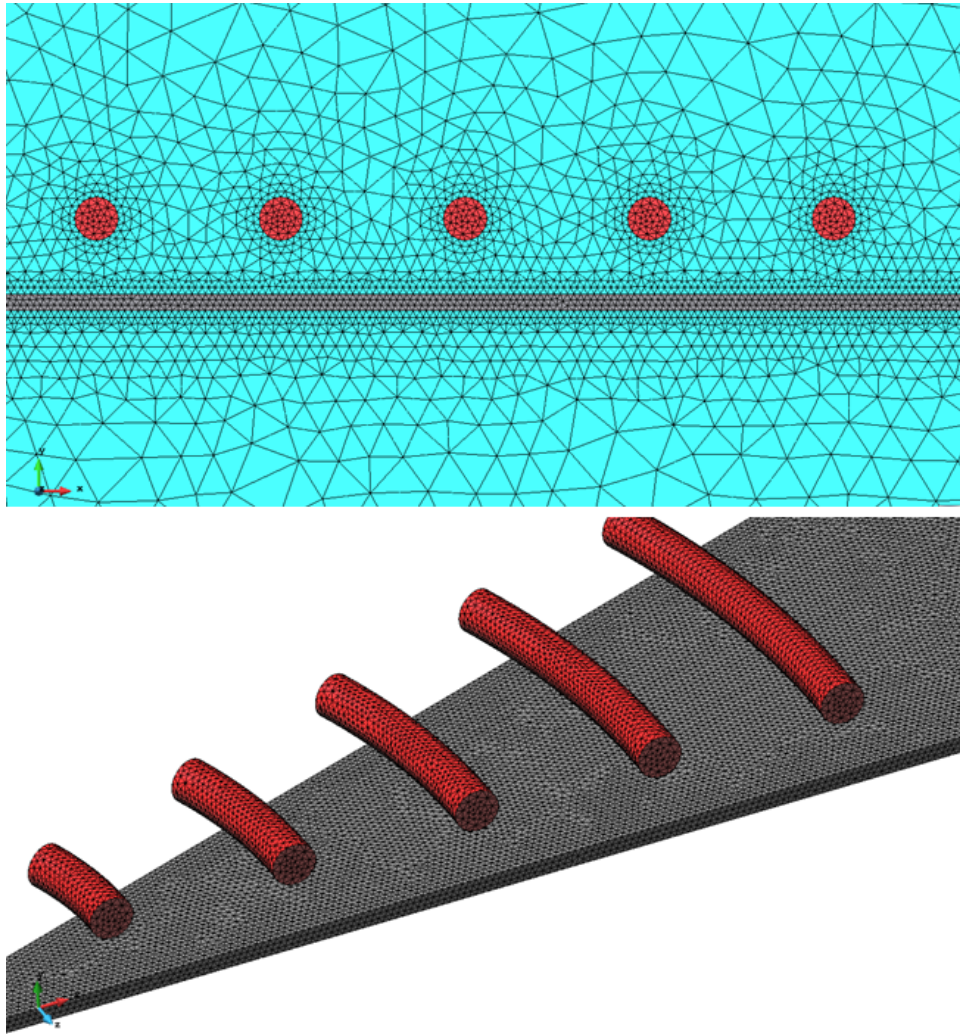


Figure 4: Details of the FEM mesh used in ERMES. The mesh consists of 529189 second order isoparametric nodal finite elements.

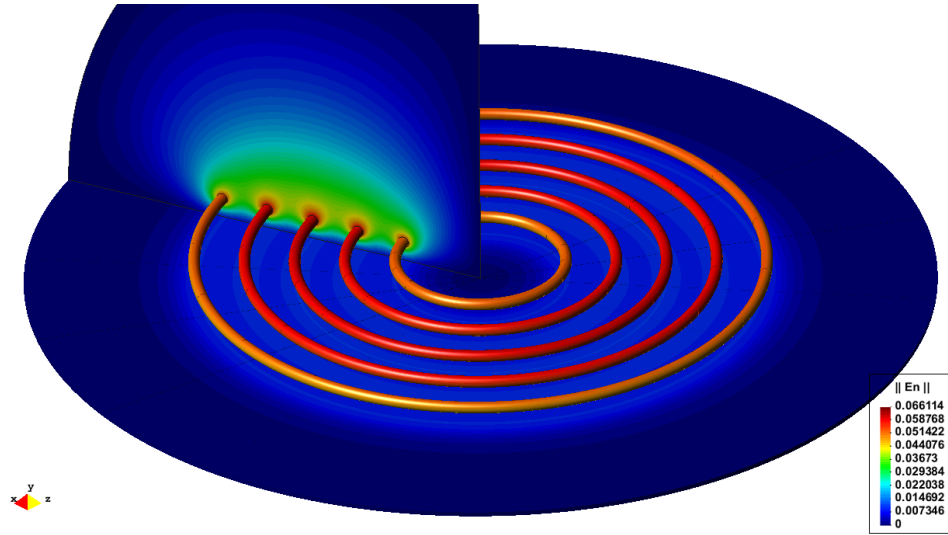


Figure 5: Modulus of the electric field per unit intensity  $\mathbf{E}_n$  at  $\nu = 16.35$  kHz.

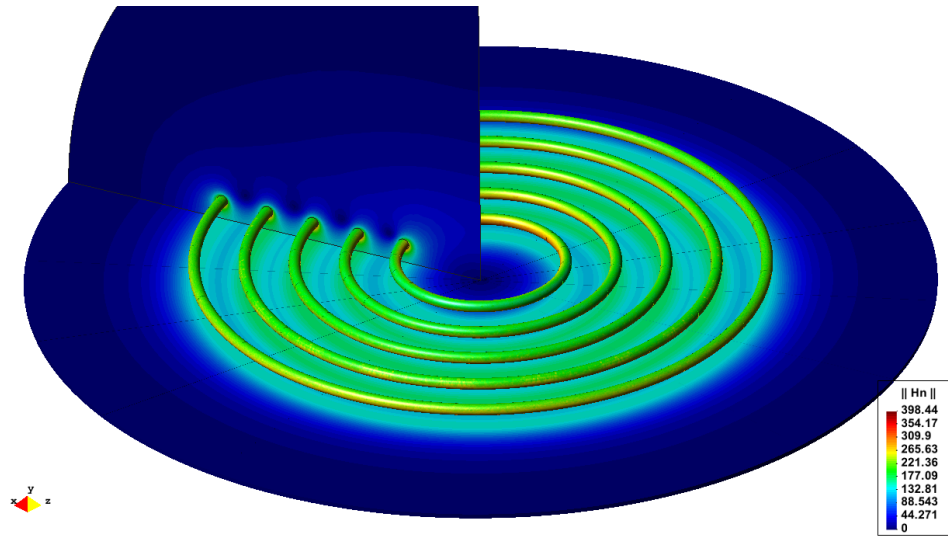


Figure 6: Modulus of the magnetic field per unit intensity  $\mathbf{H}_n$  at  $\nu = 16.35$  kHz.

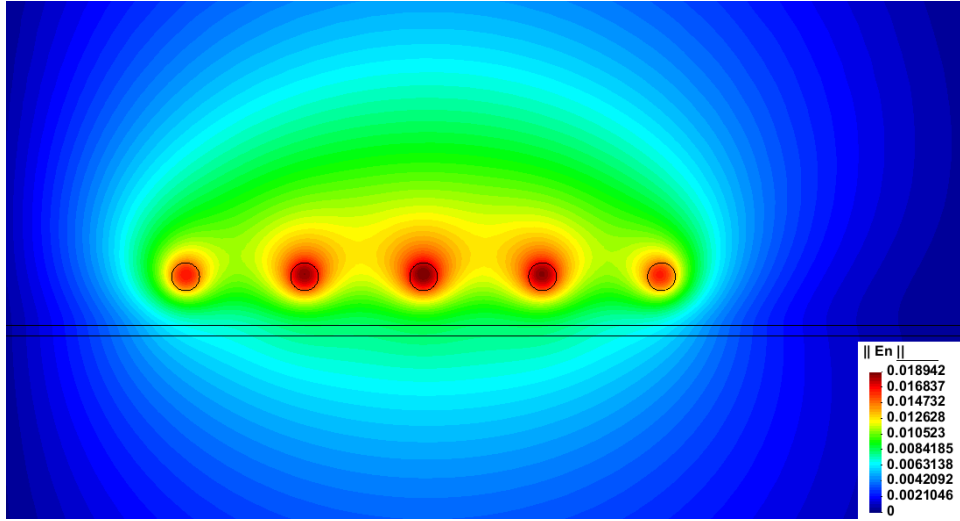


Figure 7: Modulus of the electric field per unit intensity  $\mathbf{E}_n$  at  $\nu = 4$  kHz.

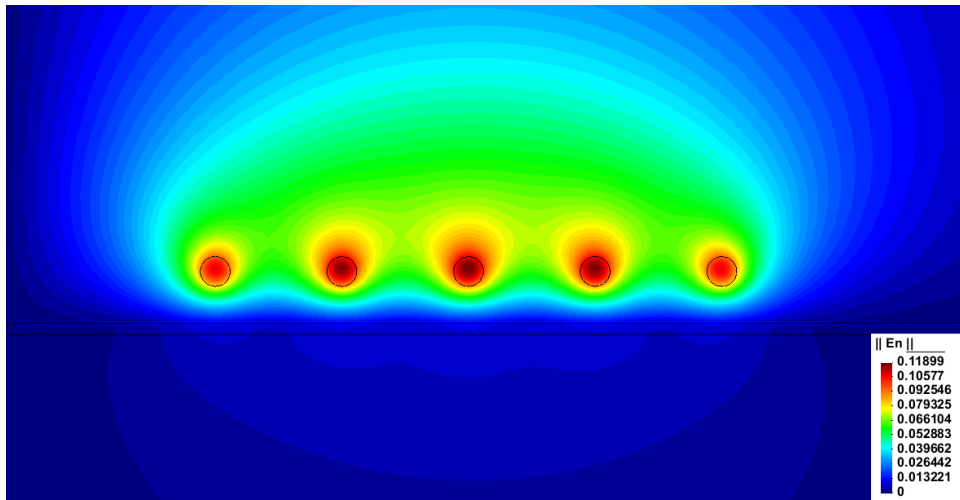


Figure 8: Modulus of the electric field per unit intensity  $\mathbf{E}_n$  at  $\nu = 30$  kHz.

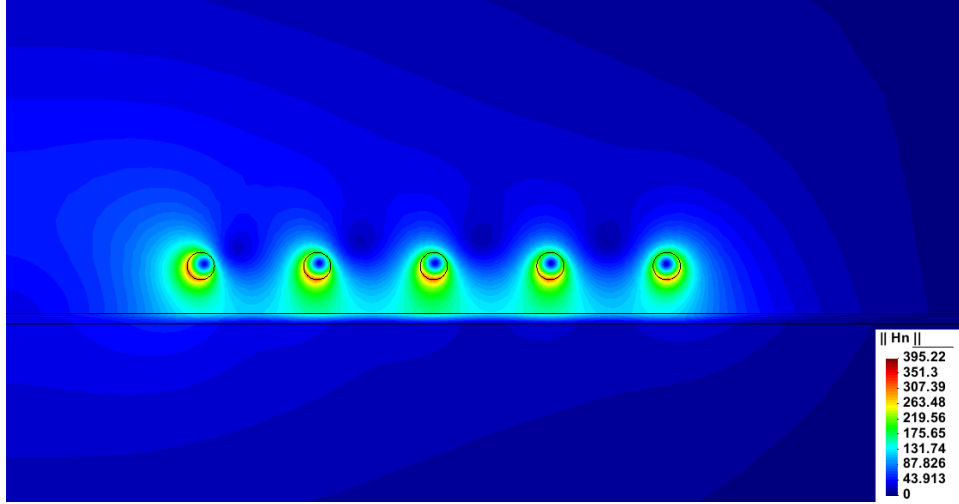


Figure 9: Modulus of the magnetic field per unit intensity  $\mathbf{H}_n$  at  $\nu = 4$  kHz.

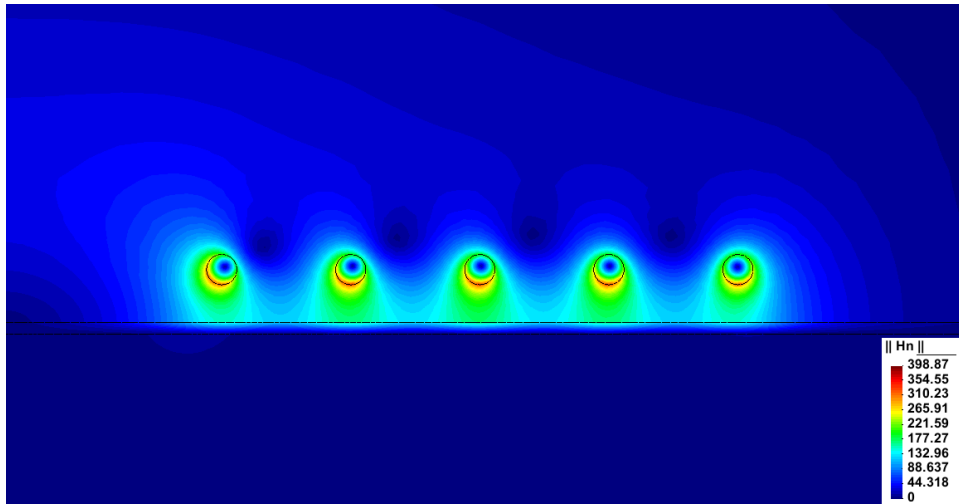


Figure 10: Modulus of the magnetic field per unit intensity  $\mathbf{H}_n$  at  $\nu = 30$  kHz.

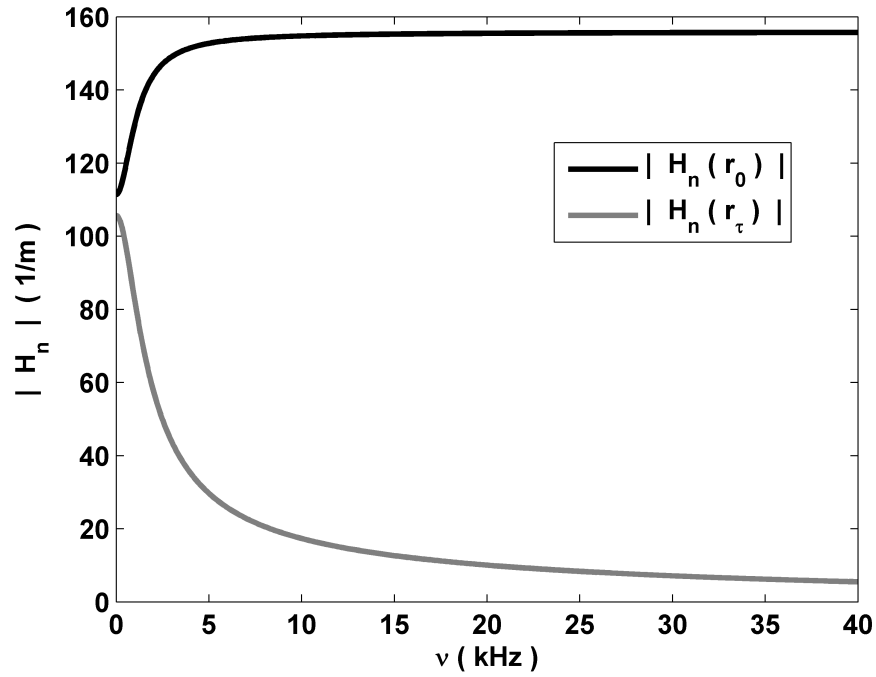


Figure 11: Modulus of the magnetic fields per unit intensity  $\mathbf{H}_n(\mathbf{r}_0, \omega)$  and  $\mathbf{H}_n(\mathbf{r}_\tau, \omega)$  as a function of the frequency  $\nu = \omega/2\pi$ . The point  $\mathbf{r}_0$  is located on the work piece surface facing the coil. The point  $\mathbf{r}_\tau$  is located on the opposite side of the work piece, on the surface farthest to the coil, diametrically to  $\mathbf{r}_0$ .

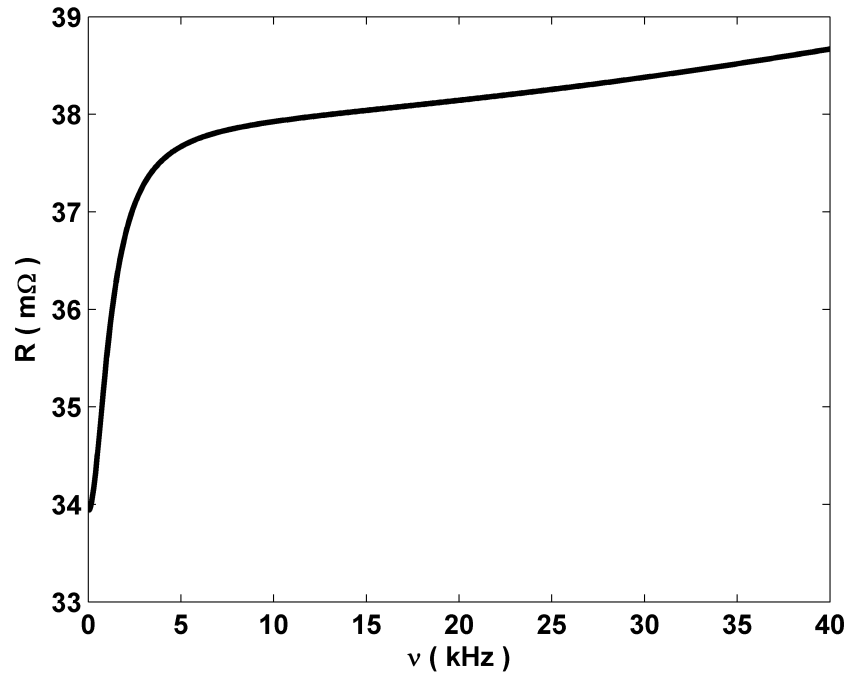


Figure 12: Total resistance  $R_0 = R_{cb} + R_{con} + R_{cw}$  as a function of the frequency  $\nu$  for the un-deformed work piece placed in its initial position. The resistance of the system *coil-work piece*  $R_{cw}$  is calculated with equation (3) in the volume of the work piece and with equation (4) in the volume of the coil. The value of  $R_{cw}$  varies from 8.4 m $\Omega$  at the lower frequencies to 13.2 m $\Omega$  at the higher frequencies. We assume that the resistance of the exterior circuit  $R_{cb} + R_{con} = 25.5$  m $\Omega$  remains constant in this frequency band.

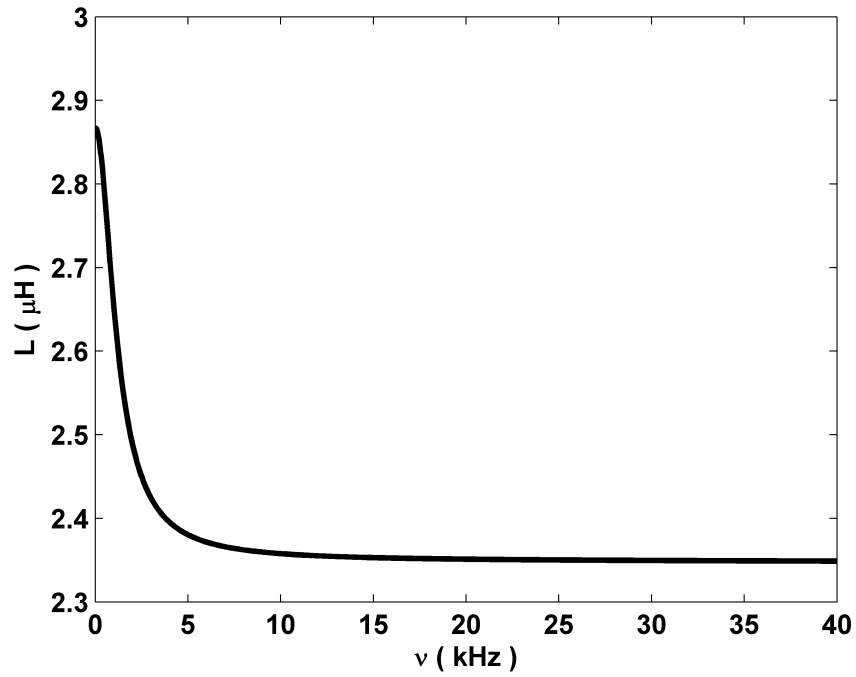


Figure 13: Total inductance  $L_0 = L_{cb} + L_{con} + L_{cw}$  as a function of the frequency  $\nu$  for the un-deformed work piece placed in its initial position. The inductance of the system *coil-work piece*  $L_{cw}$  is calculated with equation (2). The value of  $L_{cw}$  varies from  $0.86 \mu\text{H}$  at the lower frequencies to  $0.35 \mu\text{H}$  at the higher frequencies. We assume that the inductance of the exterior circuit  $L_{cb} + L_{con} = 2.0 \mu\text{H}$  remains constant in this frequency band.

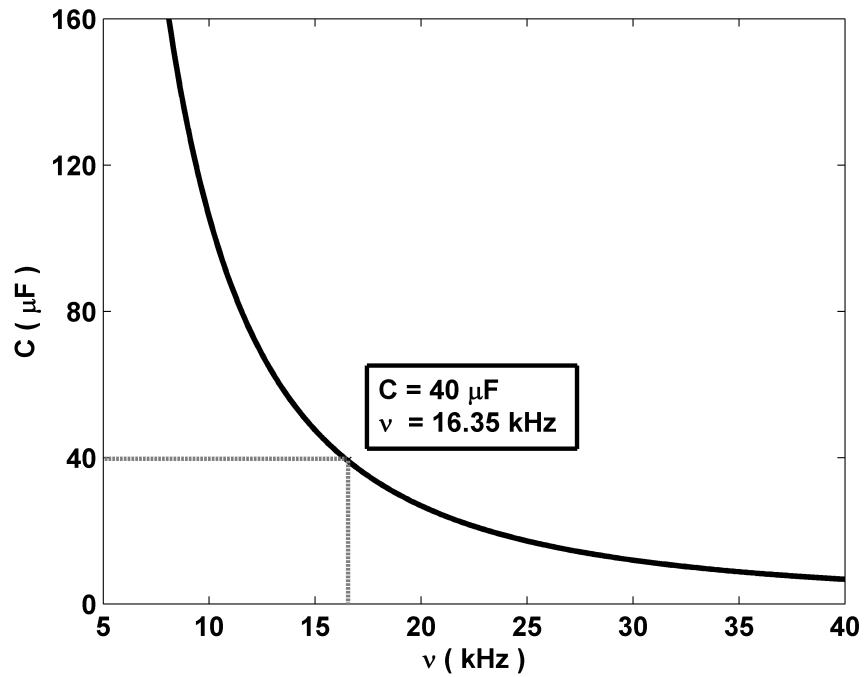


Figure 14: Capacitance  $C_0$  as a function of the frequency  $\nu$  for the undeformed work piece placed in its initial position. The function  $C_0(\nu)$  is obtained from equation (12). If the capacitor bank has a capacitance of  $C_{cb} = 40 \mu\text{F}$  then the oscillation frequency of the RLC circuit is  $\nu_0 = 16.35 \text{ kHz}$ .

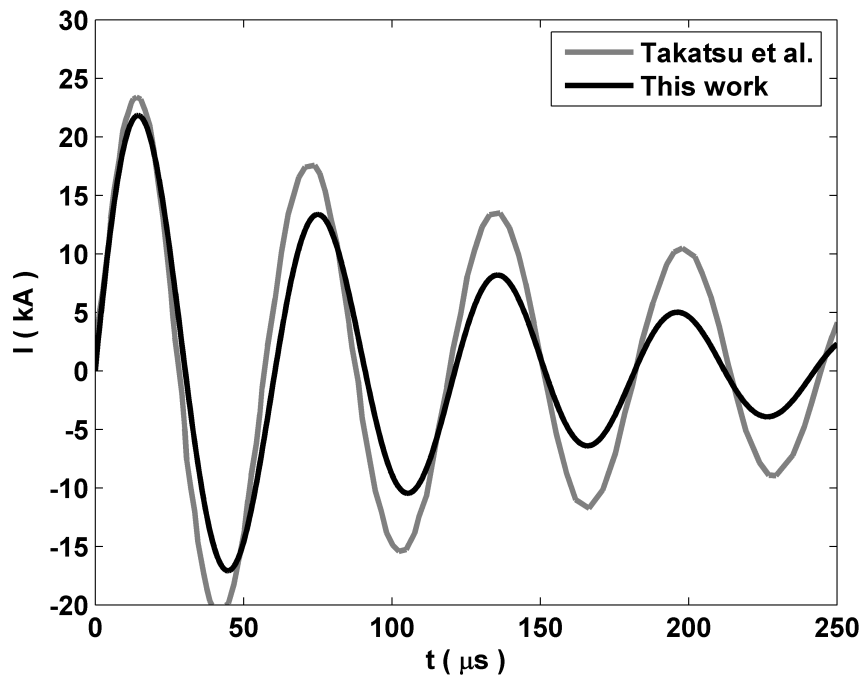


Figure 15: Current intensity simulated in Takatsu et al. [39] compared with the current intensity calculated in this work. We have graphed expression (8) with  $V_0 = 6 \text{ kV}$ ,  $C_{cb} = 40 \mu\text{F}$ ,  $\nu_0 = 16.35 \text{ kHz}$ ,  $\omega_0 = 2\pi\nu_0$ ,  $L_0 = 2.35 \mu\text{H}$  and  $R_0 = 38.1 \text{ m}\Omega$ .

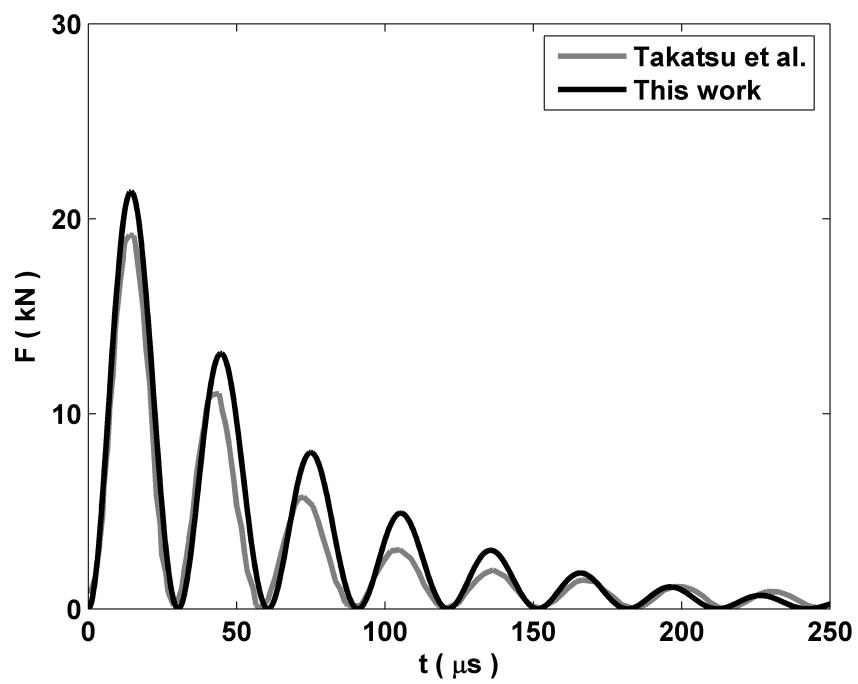


Figure 16: Total magnetic force simulated in Takatsu et al. [39] compared with the total magnetic force calculated in this work.

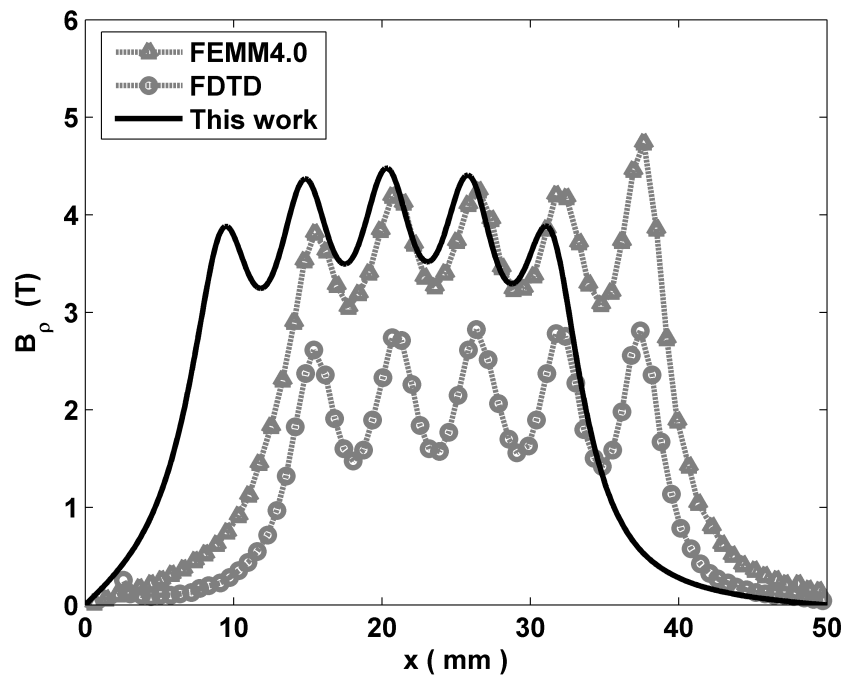


Figure 17: Radial component of the magnetic flux density simulated in [35] with FEM (FEMM4.0) and FDTD compared with the radial component of the magnetic flux density calculated in this work with ERMES.

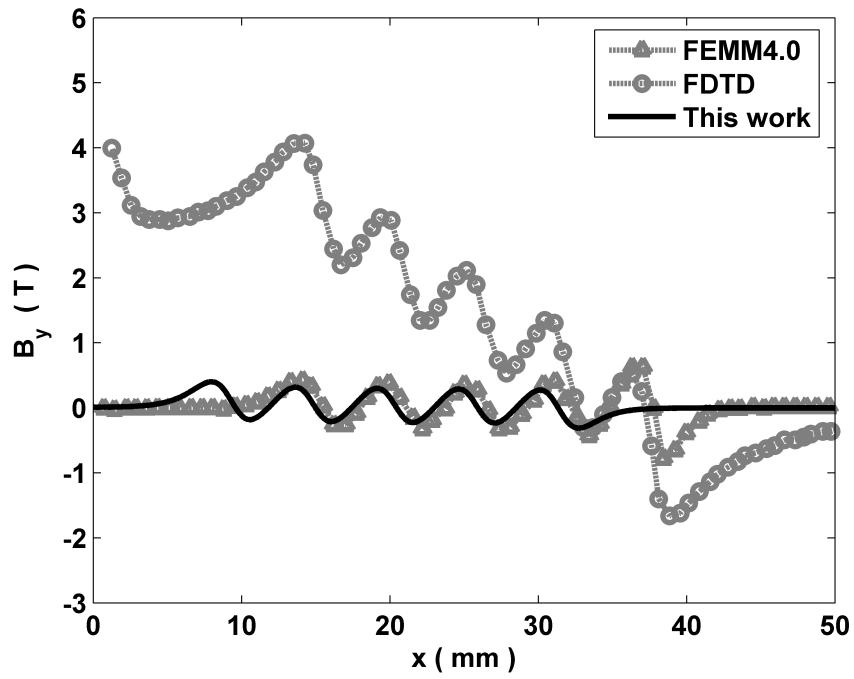


Figure 18: Axial component of the magnetic flux density simulated in [35] with FEM (FEMM4.0) and FDTD compared with the axial component of the magnetic flux density calculated in this work with ERMES.

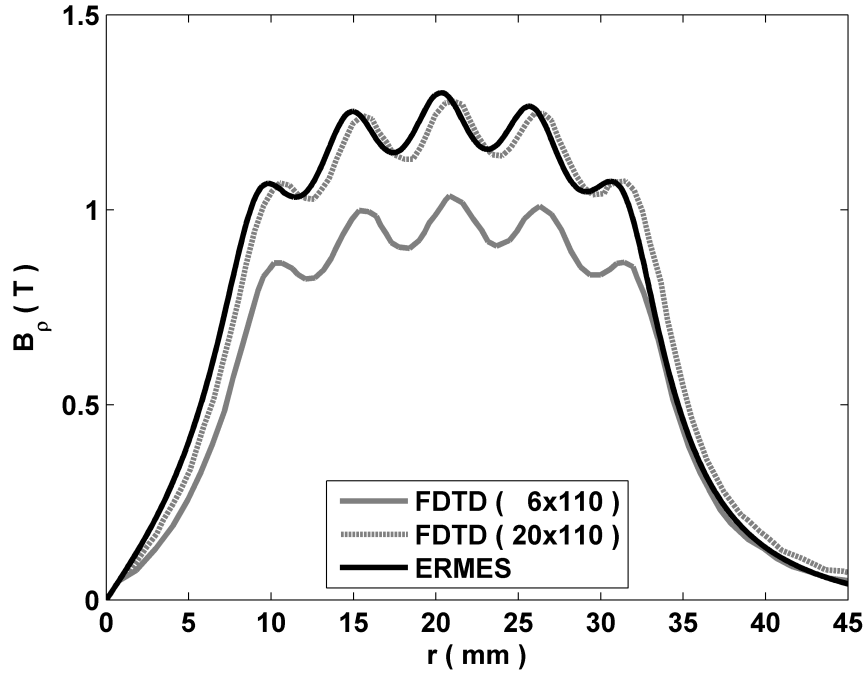


Figure 19: Radial component of the magnetic flux density  $B_\rho$  for the same coil as displayed in Fig. 2, but with a fixed work piece of thickness  $\tau = 3.0$  mm, gap distance  $h = 2.9$  mm and initial voltage  $V_0 = 2$  kV. FDTD (6x110) represents the simulations performed in [34] with a FDTD mesh of 6 elements along the thickness of the sheet and 110 elements along the radial direction. FDTD (20x110) represents the simulations performed in [34] with a FDTD mesh of 20 elements along the thickness of the sheet and 110 elements along the radial direction. ERMES represents the simulations performed in this work.

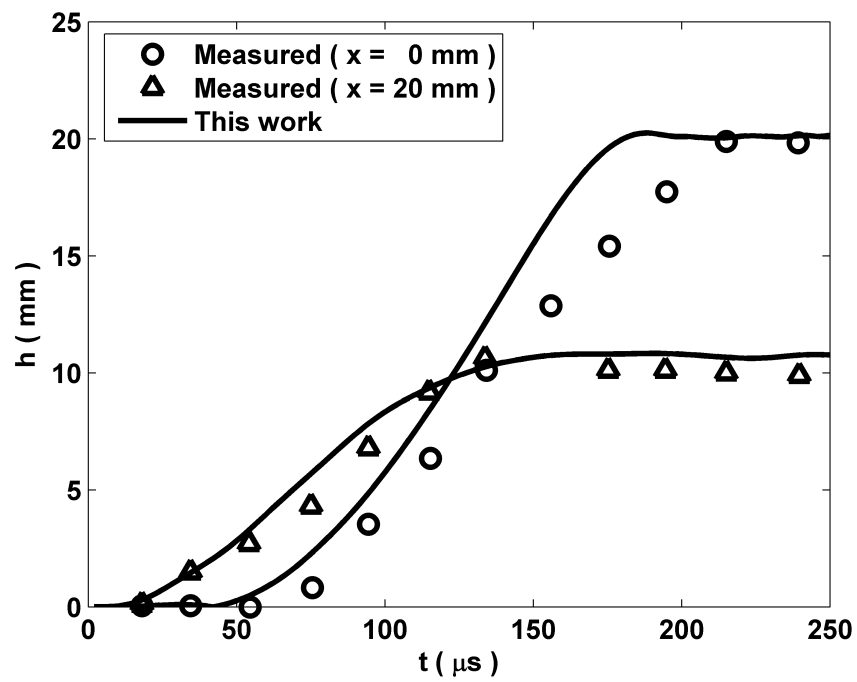


Figure 20: Deformation of the work piece at the positions  $x = 0$  mm and  $x = 20$  mm as a function of time. The results of this work are compared with the measurements of Takatsu et al. [39].